On the wavy flow past a weakly submerged horizontal circular cylinder at low Keulegan–Carpenter numbers

Guido Lupieri[1] · **Giorgio Contento**[1]

Accepted: 24 February 2017

Abstract The interaction of regular waves with a weakly submerged horizontal circular cylinder at Keulegan–Carpenter *KC* numbers up to 2.5 is studied by means of numerical simulations, solving the two-phase flow Navier–Stokes equations with the Finite Volume method and the Volume of Fluid interface capturing method. Experimental data from laboratory tests conducted in the past by one of the authors are used as reference data. The study is focused on the surface wave transformation, on the flow field in the near region and on the loads on the cylinder. The interest is driven on the spectral content of the transmitted waves at higher order frequencies and on the non-linear features of the wave reflected by the cylinder. The flow field in the near-body region is analyzed in terms of vortex onset, development and detachment, and correlating pressure pulses with the vorticity field at the cylinder surface. Inviscid flow simulations are carried out too, to evince the origin of higher order terms either from the free surface or from the viscous terms in the momentum equations. The steady streaming around the cylinder is analyzed, including its variability along the cylinder surface and its relationship with the vortex cores generated at the body surface.

Keywords Non-linear wave-body interaction · Low Keulegan–Carpenter numbers · Circular cylinders · Experimental and numerical investigation · Vorticity field

✉ Guido Lupieri
glupieri@units.it

[1] Department of Engineering and Architecture, University of Trieste, via Valerio, 10, 34127 Trieste, Italy

1 Introduction

The study of wave-induced forces on submerged objects is traditionally one of the fundamental topics related to the design of complex marine and offshore structures. For this reason, the problem of the fluid-body interaction in the case of a 2D orbital flow around a fully submerged cylinder or in the case of a wavy flow past a weakly submerged horizontal circular cylinder with its axis parallel to the incoming wave crests has been faced by many researchers. The physics is notoriously rich, and in the following, we report some of its aspects and related literature of interest for the present work. They are arranged according to inviscid and viscous approach, respectively, also mentioning the presence of experimental data sets. The target of these studies mainly covers two subjects: diffraction and viscous effects.

In the inviscid flow scenario, Dean [12] showed that at the first order, there is no reflected wave by the cylinder and the transmitted wave undergoes a phase shift only, confirmed later on by experimental results from others.

Ogilvie [26], Vada [40], and Wu and Eatock Taylor [41] derived the expression for the second-order diffraction force by a perturbation expansion. From these analyses, second-order effects were directly related to the submergence of the cylinder.

Yeung and Vaidhyanathan [42] studied the fully non-linear diffraction of water waves by a cylinder with a body fitted finite-element method, for various wavelengths and amplitudes of the incident wave, for diffraction parameter ka greater than 0.4, where k is the wave number and a is the cylinder radius. Their simulations were meant to reproduce experimental data from Chiu [7], the submergence of the cylinder axis being one diameter or less, and those from Grue and Granlund [15], with different wave slopes. The presence of evanescent modes generated by

the wave-maker was observed very close to the cylinder on the weather side. The generation of higher order waves at the lee side of the cylinder was clearly shown with a good reproduction of the experimental data. The saturation of the second harmonic component with increasing wave steepness observed experimentally by Grue and Granlund [15] was also well captured.

Contento and Casole [10] showed a reasonable agreement with the results of Chiu [7] up to the wave breaking limit, using a Mixed Eulerian Lagrangian method with a Boundary Integral formulation [9].

Schonberg and Chaplin [35] adopted an indirect Desingularized Boundary Integral Equation Method with fully non-linear free surface boundary conditions to study the transmission and reflection of waves by a submerged cylinder, both in deep and shallow water. From their computations, they found that in deep water, transmitted wave amplitudes behave at fourth order, at the first order in shallow water.

In the viscous simulations or experimental scenario, Longuet-Higgins [21], Riley [31, 32] showed that a thorough modification of the external inviscid flow derives from the non uniform oscillatory nature of the boundary layer around the cylinder that, in turn, induces a steady streaming around the cylinder surface.

Chaplin [1, 2] conducted experimental tests measuring both the forces acting on the cylinder and the fluid velocity field in a region close to the cylinder surface. His results demonstrate the strongly non-linear behavior of the loads for Keulegan–Carpenter numbers *KC* less than 3. He also observed that wave reflected by the cylinder is very small, up to 4% only for the steepest wave used. On the lee side, transmitted waves were shown to undergo a clear phase change, the values being comparable to the result of the linear solutions only for the smallest wave amplitudes. The phase change then reduces progressively while increasing the incident wave amplitude. For the steepest waves, the order of magnitude of the second harmonic was shown to be around 20% of the first.

Stansby and Smith [37] applied the random vortex method to the interaction between the cylinder and an onset orbital flow. Among the results, evidence was given to the strongly unsymmetrical structure of the vorticity around the cylinder, with a concentration region that covers almost half cylinder surface and lags the incident unperturbed velocity vector at the cylinder axis by 90° approximately. This asymmetry induces a force in opposition to the common inertia force. They also showed that the flow exhibits an increasing complexity with increasing *KC* and a poor steady-state behavior of the forces is reached when *KC* approaches 2.

Grue [14] experimentally studied the interaction of an horizontal circular cylinder with regular waves. The analysis is referred to wavelength to diameter ratios between 3 and 8 approximately, with very low *KC* numbers, less than 0.3, and mostly with a clearance between the upper part of cylinder and the calm water level always less than one cylinder radius. His results showed that higher order harmonics in the free surface elevation, averaged over different stations, appear mostly on the lee side. This effect corresponds to a large transfer of energy from the incoming wave to the higher order free waves up to 25%. It was also found that the amplitude of the higher order components generated at the cylinder exhibits a kind of saturation as the incoming wave amplitude is progressively increased.

Otsuka and Ikeda [30] presented some visualizations of the flow, giving experimental evidence to the separation that occurs around the cylinder when the orbital uniform flow is started from rest. From these visualizations, they derived a simplified vortex shedding model that gives a simple quadratic law in *KC* for the inertia coefficient C_m [25]. Their theoretical results are in close agreement with those derived experimentally by Chaplin [2].

Oshkai and Rockwell [29] conducted experimental tests with PIV and analyzed the interaction between a free surface wavy flow and a submerged cylinder in terms of correlation between patterns of vorticity and loads, including the effect of submergence. Their tests were conducted with *KC* around 7. They showed that the presence of the free surface can exert a remarkable influence on the initial formation, the strength, and the subsequent motion of concentration of vorticity.

Contento and Codiglia [11] conducted experimental tests on the interaction of regular waves past a submerged horizontal circular cylinder with different values of the submergence of the cylinder axis, respectively, 2, 3, and 4 radii. The *KC* range investigated in the experiments is between 0.1 and 2.5, with a nominal Reynolds number *Re* of order of 10^4. The diffraction parameter *ka* was varied between 0.125 and 0.52. Wave loads were obtained by pressure integrals over a large number of pressure probes, assuming that for such blunt body and at these *KC* and *Re*, the tangential stress is orders of magnitude lower than the normal stress. Their results are in full agreement with those obtained by direct measurement of the force by Chaplin [1, 2] and those obtained by Grue [14], both in terms of non-linearities of the forces and of the free surface behavior. Among the results, they showed that second and third Fourier components of the pressure and of the free surface elevation in a wide portion at the lee side of the cylinder are strongly dependent on the submergence of the cylinder, whereas the first harmonic is only weakly dependent on it, consistently with the *ka* values used.

Chaplin [6] conducted a series of experiments aimed at the identification of the non-linear features of wave interaction in the presence of a weakly submerged cylinder for

a wide range of the diffraction parameter ka and varying the incident wave amplitude up to breaking, comparing the results to inviscid flow solutions from the literature. In diffraction regime, second-order solutions were shown to give excellent results in terms of wave profile on the lee side of the cylinder, necessarily without breaking. Higher frequencies up to the fifth were also detected in the measured wave elevation profile. The mean wave elevation above the cylinder was also derived from the measurements and checked against theoretical prediction with good results up to the breaking condition. Finally, transmitted waves at the first, second, and third harmonics were studied carefully, specifically their dependence on the incident wave amplitude. It was found that the second and third harmonics behave as a power of 2 and 3, respectively, plus a contribution in the 4th and 5th powers of the incident wave amplitude. As far as the first harmonic is concerned, correspondingly to the results of Chaplin [1], it was found that a strong third-order term is related to the steady streaming around the cylinder. From the rapid decay of the quality of the results obtained with a simplified vortex line model for a shallower and shallower cylinder, it was argued that the closer to the free surface the cylinder is, the less uniform the circulation around the cylinder becomes, with large values of circulation on the top of the cylinder.

From the literature above, it can be summarized that non-linear inviscid flow solutions can be used rather successfully to simulate the free surface behavior, with limitations given by wave breaking. On the other hand, these solutions give pressure forces on the cylinder that are missing higher order terms, even at the fundamental frequency. Viscous effects, steady streaming in particular, are recognized to be responsible of these non-linearities, even at relatively small KC numbers. The resulting velocity field patterns are, therefore, complex, with a non uniform streaming and ultimately eddies detachment.

The present work tackles this problem by solving in 2D the two-phase flow Navier–Stokes equations. In particular, the purpose is to analyze the non-linear features of the waves passing over the cylinder and of the pressure at the cylinder surface, evidencing the contributions that come from the inviscid and viscous part of the flow, specifically in relationship to eddies that are detached from the cylinder, mostly at low submergences and with breaking. Wave elevation and pressure at the cylinder are analyzed by comparing the results with experimental data previously obtained by one of the authors [11]. Higher order terms are analyzed and directly referred to specific features of the flow field. The study is conducted following the assumptions of the experimental work used as reference: the incident wave height H and the cylinder submergence y^*/a are considered as main independent parameters; increasing appropriately both y^*/a and H, and keeping the wavelength fixed, they provide the same KC number with the same diffraction parameter ka. The analysis of the simulations conducted keeping fixed the diffraction parameter ka and the submergence y^*/a, while varying the ratio between the incident wave height and the cylinder radius is left to a further work (in preparation). Among the results, it is assessed the presence of a steady circulation around the cylinder and is defined the threshold in terms of KC number above which the flux departs from irrotational regime in regions relatively far from the submerged object and in the absence of breaking events.

The paper is organized as follows: the problem formulation is first presented and the mathematical model and numerical method are briefly summarized; the wave generation and absorption process is then described; the results include the topics of wave transformation and reflection; the analysis of the mechanism of onset and detachment of vorticity patterns from the cylinder and a measure of vorticity intensity is given; finally, the pressure loads at the cylinder surface are analyzed with specific focus on pressure pulses found in connection to the vortex detachment.

2 Problem formulation

In Fig. 1a, schematic representation of the physical problem is given, with the relevant symbols. A Cartesian frame of reference $O(x, y)$ is used with x-axis placed at the still free surface and the y-axis is upwardly oriented. The origin O is placed in correspondence of the longitudinal position of the cylinder axis. The angular coordinate θ on the cylinder surface is defined starting from the vertical position and with positive values clockwise.

Adopting a linear wave model, the nominal Keulegan–Carpenter number KC and the Reynolds number Re read as follows:

$$KC = \frac{UT}{D} = \frac{\pi H}{D}\frac{\cosh(k(y^* + h))}{\sinh(kh)} \tag{1}$$

$$Re = \frac{\rho UD}{\mu} = \frac{\rho \pi HD}{\mu T}\frac{\cosh(k(y^* + h))}{\sinh(kh)}. \tag{2}$$

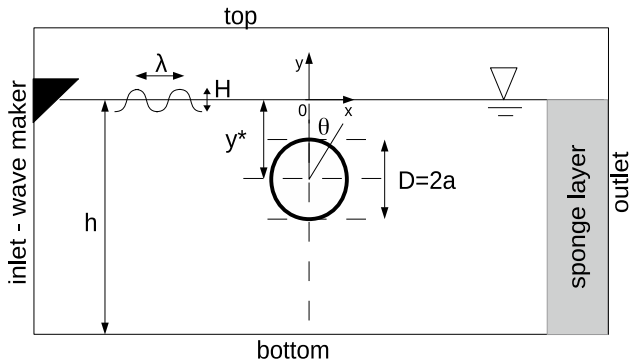

Fig. 1 Schematic representation of the physical problem, with relevant symbols

In Eqs. 1 and 2, U is the maximum velocity of the incident undisturbed flow at the cylinder axis, T is the dominant period of the incident flow, H is the wave height, λ is the incident wavelength, k is the wavenumber, $D = 2a$ is the cylinder diameter (a is the radius), y^* is the depth of the cylinder axis, and h is the water depth assumed constant; $y^*/a = -2, -3, -4$ will indicate the cylinder submergence in the rest of the text and in the figure captions. The incident waves travel in the positive x-axis direction.

In the following, $t/T = 0$ corresponds to the first zero up-crossing of the undisturbed incident wave at the cylinder axis in stationary Fourier conditions. The latter condition is not always strictly fulfilled, so the analysis is conducted over an integer number of dominant periods, starting from $t/T = 0$. Statistics (averages) are then computed over corresponding time steps $t/T + i$, where $0 \leq i < 4$. This time windows is selected free from transient effects induced typically by the wave front and by possible reflections from the absorbing beach.

The simulations conducted here and the experiments described in Contento and Codiglia [11] have been planned in such a way that the diffraction parameter ka, the nominal Reynolds Re, and Keulegan–Carpenter KC numbers are kept constant while varying the depth of the cylinder $y^*/a = -2, -3, -4$. Then, ka and KC have been varied in the ranges $0.125 \leq ka \leq 0.52$ and $0.1 \leq KC \leq 2.50$, respectively. The maximum Reynolds number Re achieved is 3.5×10^4. The cases presented here are given in Table 1: the test number corresponds to the same test number given in Contento and Codiglia [11]. The simulations cover the entire range of KC available in the experiments and with a specific interest to the complex fluid–body interaction, with wave breaking and a partial exit of the cylinder surface.

3 The mathematical model and numerical method

Without heat exchanges, the governing equations in differential form for an incompressible Newtonian fluid are the following:

$$\frac{\partial(\rho u_i)}{\partial t} + \frac{\partial(\rho u_j u_i)}{\partial x_j} = -\frac{\partial p}{\partial x_i} + \frac{\partial}{\partial x_j}\left(\mu\left(\frac{\partial u_i}{\partial x_j} + \frac{\partial u_j}{\partial x_i}\right)\right) + F_i \tag{3}$$

$$\frac{\partial u_i}{\partial x_i} = 0 \tag{4}$$

where ρ is fluid density, u_i is a velocity component, p is the pressure, μ is the dynamic viscosity, F_i are the body forces, and t and x_i are the time and space independent variables. Turbulence parameterization can be applied and Eq. 3 can be reformulated in terms of Reynolds averages, adding new equations that define the eddy viscosity.

The numerical solution of Eqs. 3 and 4 is conducted in the OpenFOAM [28] framework. This library is known and appreciated for engineering applications because of its own versatility in affording a wide class of fluid mechanics problems. This is probably due to both the Finite Volume formulation, intrinsically ensuring conservation properties, and to a number of schemes devoted to steer the solution towards stability, as for instance in the advection formulation, where it is possible to bound the solution, limiting the fluxes interpolated at the cells surfaces with bounding values. This approach results particularly useful in case of unstructured and coarse meshes in complicated flows where computed gradients can hardly lead to convergence. In spite of that, the predictor–corrector like approach for the solution of Eqs. 3 and 4—as implemented in the software—has been considered by the authors also for scientific studies after a series of tests selected to obtain reliable simulations of free surface waves. Among others:

Table 1 Test cases studied

Test #	D (m)	λ (m)	Re	KC	ka	T (s)	H (m)	$-y^*/a$
1	0.315	1.90	7937	0.10	0.5208	1.1033	0.0284/0.0478/0.0803	2/3/4
4	0.315	2.35	17836	0.25	0.4211	1.2271	0.0581/0.0883/0.1338	2/3/4
7	0.315	2.80	26123	0.40	0.3534	1.3394	0.0808/0.1145/0.1614	2/3/4
11	0.315	3.40	35462	0.60	0.2911	1.4759	0.1059/0.1403/0.1846	2/3/4
15	0.315	4.00	43372	0.80	0.2474	1.6009	0.1273/0.1606/0.2008	2/3/4
19	0.160	2.35	21721	1.18	0.2139	1.2271	0.0921/0.1140/0.1411	2/3/4
22	0.160	2.80	25947	1.54	0.1795	1.3394	0.1119/0.1338/0.1598	2/3/4
26	0.160	3.40	30803	2.02	0.1478	1.4759	0.1368/0.1582/0.1828	2/3/4
30	0.160	4.00	34969	2.50	0.1257	1.6009	0.1596/0.1805/0.2036	2/3/4

The test # corresponds to the test number given in the paper of Contento and Codiglia [11], D is the diameter of the cylinder, λ is wavelength, k wave number, a cylinder radius, T wave period, H wave height, and y^*/a the depth of submergence of the cylinder made non-dimensional with its radius

1. verifying the mass conservation in the computational domain within the VOF approach;
2. limiting the numerical dissipation with high resolution in the near wall region (ideally resolving the boundary layer), in the outer layer to capture pressure variations and at the air–water interface for the wave shape reconstruction;
3. composing the computing grid by structured blocks limiting the cells skewness;
4. imposing second-order accuracy with linear interpolation at the cell faces and no upwind in the discretization of non-linear terms (referenced in Table 2);
5. ensuring convergence in iterative algorithms;
6. preparing a suited inlet boundary condition;
7. preparing a suited numerical beach to limit reflections from the outlet boundary.

The problem faced in this work, a two-phase flow with a coupled air-water system, has been generally categorized into boundary-discretization and volume-discretization approaches by Tsai and Yue [39]: while boundary-discretization methods are mostly used for inviscid irrotational flows, volume-discretization approaches are more generally applicable to both inviscid and viscous flows. Concerning the volume-discretization methods, in the Eulerian-grid formulation, the field equations can be solved in an inflexible grid system with the major advantage in the robustness in case of complicated geometries of the boundary. An example of this method is VOF, the interface capturing method by Hirt and Nichols [18] here adopted, in which a scalar function α, with $0 \leq \alpha \leq 1$ represents the phase of the fluid in each cell (0 = air, 1 = water).

After Rusche [34], a modified transport equation has been adopted with an additional convective term that keeps the interface sharp even with the step-like nature of α; thus, the modified substantial derivative of the scalar function α reads:

$$\frac{\partial \alpha}{\partial t} + \frac{\partial (u_i \alpha)}{\partial x_i} + \frac{\partial (w_i \alpha)}{\partial x_i} = 0 \tag{5}$$

where w_i is an artificial velocity field that is directed normal to and towards the interface. The relative magnitude of the artificial velocity is determined with the following expression:

$$w_i = K_c n_i^* \max \frac{|n_i^* F_l|}{|S_i|} \tag{6}$$

where K_c is an adjustable coefficient (here set equat to 1) that determines the magnitude of the compression, n_i^* is the interface unit normal vector, F_l is the flux, and S_i is the surface area vector.

Equations 3–5 are solved within a Finite Volume framework, using the schemes summarized in Table 2, with a second-order Gaussian integration.

The pressure-velocity coupling is achieved using a Pressure Implicit with Splitting of Operator (PISO) algorithm. The Euler explicit scheme is adopted to march forward in time. The free surface location is computed using the Multidimensional Universal Limited for Explicit Solution (MULES) method.

The 2-D computing domain is $N_b \lambda$ long before the cylinder and $N_a \lambda$ after the cylinder axes in the longitudinal direction, with $N_b = 4.5$ and $N_a = N_b + 2$. The water depth is constant and equal to $h = 1.550 \pm 0.002$ m, consistently with the experiments. As far as the grid is concerned, the air–water interface zone is discretized vertically with 80 cells over the highest expected wave height. The first computing node at the wall of the cylinder has been placed at $y^+ = 1$. The grading to the outer layer is imposed according to standard ITTC recommendations on CFD in Marine Hydrodynamics [27]. The total number of cells is around 1.8×10^6 cells and the computations have been conducted over a dedicated 48 cores system. The 3-D computing domain maintains the longitudinal and vertical dimensions, while the spanwise is 1.5 m long in consistence with the experiments of Contento and Codiglia [11]. The first computing grid node at the wall lays at $y^+ \approx 30$. In this case, parts of the grid are unstructured, with 26 M cells overall computed on a 96 cores system.

The output data have been re-sampled with 90 intervals per dominant wave period and average values have been then computed over corresponding time steps $t/T + i$, where $0 \leq i < 4$.

In case of wave breaking, occurring mostly at $y^*/a = -2$ for $KC \geq 0.8$, a turbulent regime, with bubbles and air entrainment, is present locally at the air-water interface above the cylinder. In this limited area, a turbulence model could be adopted, since the smallest scales of the phenomenon are presumably not sufficiently sampled with the resolution adopted. The discussion on this subject is huge and the literature is wide. The most common models in the RANS approach are actually not suited for this specific application (2-D flow, air-water interface, turbulence regime localized only in restricted areas) and, moreover,

Table 2 Numerical schemes in use in the simulations

	Term	Discretization
Gradient	∇	Gauss linear
Convection	$\nabla \cdot (\rho \phi U)$	Limited linear
	$\nabla \cdot (\phi \alpha)$	Limited linear
	$\nabla \cdot (\phi_{rb} \alpha)$	Interface compression
Laplacian	∇^2	Gauss linear corrected

this could lead to a lack of accuracy for instance in the prediction of the breaking wave shape or its position, basically because of an overestimation of the eddy viscosity [22]. For these reasons, in the present study, a $k-\omega$ SST turbulence model and a wall model have been adopted only in the 3-D case simulated.

4 Wave generation and absorption

Some aspects on the generation of high-quality waves and their absorption in a closed basin are key points both in numerics and experiments; among others, the generated progressive waves must fulfill a target amplitude spectrum and this depends on the characteristics of the wave-making boundary. Furthermore, evanescent modes may be induced by the wave-making boundary and partially reflected waves can be induced at the other boundaries by a not perfect absorption [13]. These effects may pollute the incident wave train and the wave–body interaction.

For these reasons, a calibration process is strongly recommended [38]. In the present work, wave conditions presented in Table 1 have been previously simulated and calibrated without cylinder.

As far as the wave generation is concerned, OpenFOAM library has recently been enriched with specific packages for wave generation. Among the others, the contributes of Jacobsen et al. [20] and Higuera et al. [17] are worth mentioning. In the present work, we have adopted our own wave-making procedure. A boundary condition, based on the Airy model, is applied at the wave-making boundary, modified with a transfer function, such that the target wave height is attained at the cylinder's axis station. Therefore, the initial conditions consist of an unperturbed flat free surface; a zero normal derivative for the pressure is prescribed at the inlet and outlet, while a constant total pressure is assigned at the top boundary; the fixed values of the velocity field are specified at the inlet boundary. Due to the inconsistency between theoretical small amplitude Airy waves and finite amplitude simulated waves, this boundary condition does not ensure a quasi zero mass transport over a complete cycle, so an additional modification of the boundary condition has been implemented to optimize the net flux at that boundary. As an example, Fig. 2a shows the wave record in the absence of submerged body for one of the cases presented. The spectral analysis (Fig. 2b) is conducted, and the iterative calibration process starts, ensuring that the wave exhibits the target parameters at the target longitudinal position. Waves attained by the simulations are actually close to Stokes waves. For instance, the second harmonic of the corresponding Stokes wave of Fig. 2b has an amplitude of 0.0032 m, while the second harmonic of the simulated wave has an amplitude of 0.0033 m.

Concerning mass conservation, the volume of water variation vs time is shown in Fig. 3, related to Test # 15 of Table 1. Oscillations are due to the wave-maker forcing, and the mean, here calculated over the last (four) full periods, tends to vanish.

As for the wave absorption, the so-called sponge layer technique has been adopted here. The characteristic feature of this method is that, to some extent, there is no need to specify the spectral content of the incident wave train. The method thus works rather efficiently also for non monochromatic waves provided that the beach length L is set longer than the typical (longest) wavelength in the wave train [8, 24] ensuring a good performance for the shorter

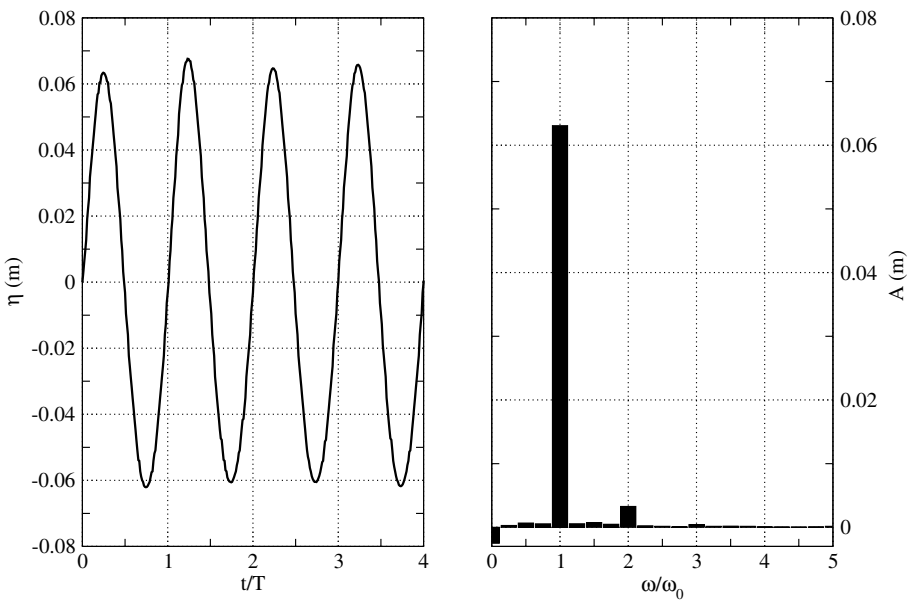

Fig. 2 Test case # 15, $y^*/a = -2$ of Table 1: *left* time record of the wave elevation at $x/a = 0$ without the submerged cylinder; *right* amplitude spectrum of the signal

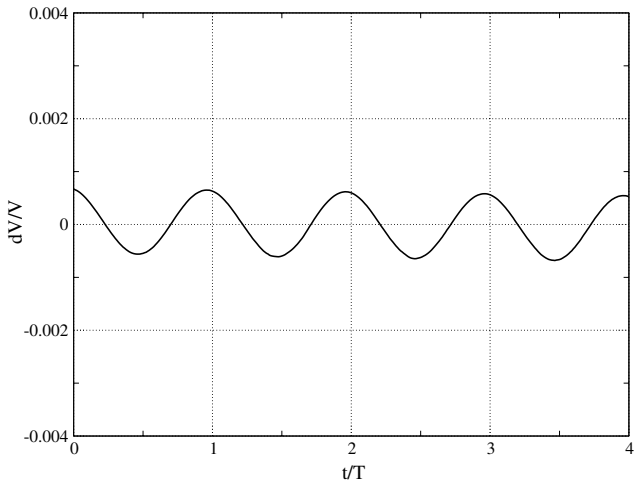

Fig. 3 Test case # 15, $y^*/a = -2$ of Table 1: volume variation vs time without the submerged cylinder

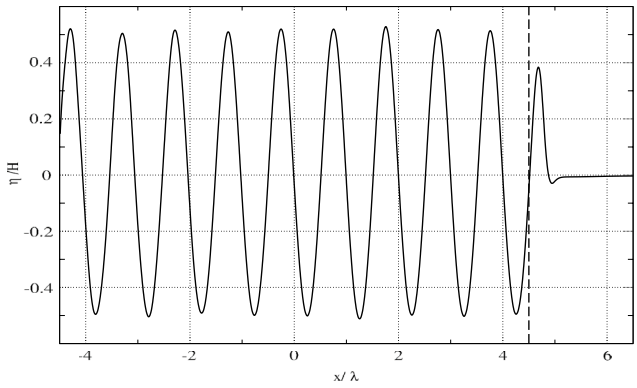

Fig. 4 Test case # 15, $y^*/a = -2$ of Table 1: snapshot of the wave elevation along the numerical tank without the submerged cylinder: absorbing layer outside the *dashed vertical line*

waves too. Equation 3 is thus modified by adding an artificial damping term enabled only on a specified zone upwind the outlet boundary:

$$\frac{\partial(\rho u_i)}{\partial t} + \frac{\partial(\rho u_j u_i)}{\partial x_j} = -\frac{\partial p}{\partial x_i} + \frac{\partial}{\partial x_j}\left(\mu\left(\frac{\partial u_i}{\partial x_j} + \frac{\partial u_j}{\partial x_i}\right)\right) + F_i - \rho\alpha\nu_{\mathrm{d}}(x)u_i. \tag{7}$$

The artificial viscosity ν_{d} in Eq. 7 is function of the longitudinal position x; it is set to zero at a given location x_{start} in the domain and goes to its final value at the outlet. The function $\nu_{\mathrm{d}}(x)$ is varied smoothly at the beginning of the sponge layer, so that reflections are minimized at that position. Here, a cubic polynomial has been used:

$$\nu_{\mathrm{d}}(x) = \begin{cases} 0 & \text{if } x < x_{start} \\ a(x - x_{\mathrm{start}})^3 + b(x - x_{\mathrm{start}})^2 + c(x - x_{\mathrm{start}}) & \text{if } x > x_{\mathrm{start}} \end{cases} \tag{8}$$

and $a = 2(\nu_{\mathrm{d,max}} - ML)/(-L^3)$, $b = -\frac{3}{2}aL$, and $c = M$.

The starting location of the sponge layer x_{start} and $\nu_{\mathrm{d,max}}$ is user specified.

The intensity of the artificial viscosity ν_{d} depends upon the amount of the wave energy to be dissipated, and therefore, it must be tuned.

In the present simulations, the following setup has been used $\nu_{\mathrm{d,max}} = 120$, $L = 2\lambda$, and $M = 0.01$.

Figure 4 shows a snapshot of the wave elevation vs the longitudinal position as obtained from one of the cases analyzed in the absence of the cylinder. The absorbing beach starts at the dashed vertical line. The reflection coefficient, computed according to the linear approach of partially reflected waves [13], was never greater then 7% in the cases simulated.

Even if wave reflection is small, to ensure additional accuracy to the results and assuming the linear wave group velocity as a reference, a time window for data analysis has been selected in an interval of 4 full periods, free from outlet and inlet boundary reflections.

5 Two-dimensional approximation

Since the computing cost of the 3D numerical experiment referenced in Sect. 3 results at the moment not affordable for the authors when all the tests in Table 1 have to be reproduced, the 2D approximation of the flows has been here considered after appropriate caveat.

Flows over circular cylinder exhibit three-dimensional features even in the absence of a relatively close free surface and even at Reynolds numbers smaller than those here faced. In particular, for $KC \geq 0.8$ and at all the submergence of the cylinder, three-dimensional instabilities and even turbulence (for instance due to breaking) can affect free surface elevation and pressure at the cylinder or, at least, differently from the 2D cases, fluctuations from a mean value are simply present in the spanwise direction of the 3D flow. For this reason, it is difficult to read the results obtained within a 2D approximations in more general terms.

However, for the mentioned quantities, the bulk flow remains mainly driven by the imposed wavy boundary conditions and the fluctuation can contribute for a few points in percentage. As an example, Fig. 5 refers to Test # 30 of Table 1 with $KC = 2.5$ and $Re \simeq 35{,}000$, $y^*/a = -3$, 3D simulations. It shows the free surface elevation at $x = a$ along the spanwise direction (Fig. 5a); Fig. 5b shows the fluctuation from the mean value in the same direction, while Fig. 5c shows the elevation produced in the corresponding 2D simulation. In this last case, the signal exhibits the presence of noise difficulty associated with the fluctuation field of the 3D case, but its presence suggests that

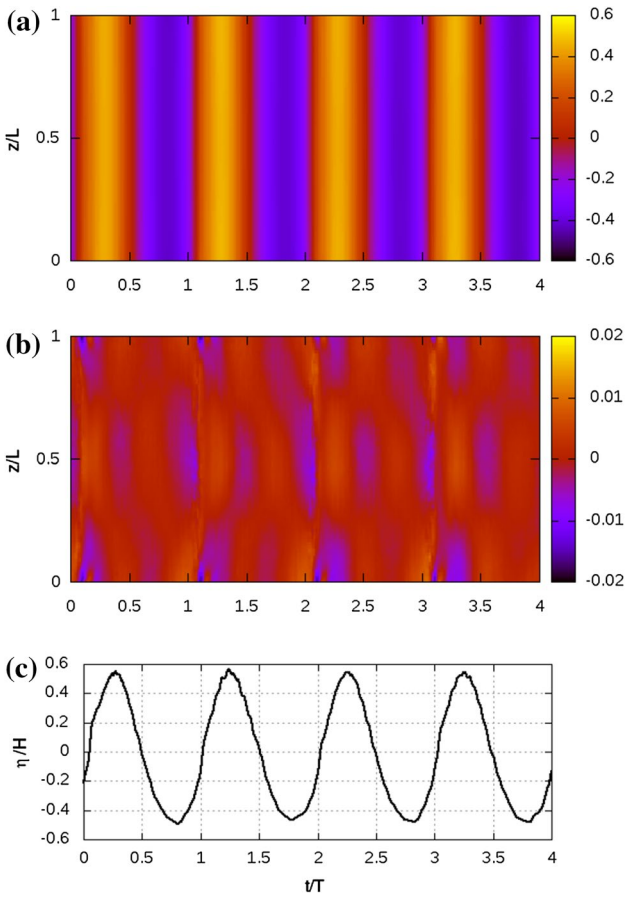

Fig. 5 Test case # 30, $y^*/a = -3$ of Table 1: **a** non-dimensional free surface elevation at $x = a$ for four selected wave periods, **b** its fluctuation from the average; **c** free surface elevation at $x = a$ in the corresponding 2D case

the analysis of the results should be addressed towards a statistical approach (averaging along the highest possible number of wave periods) and in the framework of the Fourier analysis ideally to separate the higher order harmonics from noise and, finally, to back the results with experimental data. In this way, the results of the numerical analysis within the 2D approximation will be considered here acceptable for free surface elevation and pressure at the cylinder (loads). This part is discussed in Sect. 6.

Otherwise, the 2D approach can affect vortices pattern kinematics around the cylinder: this topic has been covered for instance by Lupieri and Contento [23] where the typical matching of vorticity dipoles with opposite sign has been shown, consistently with the inverse energy-cascade mechanism. For this reason, in the following sections, the vorticity analysis will be addressed limiting the results within the 2D context, excluding a priori deep investigations on topics as the interaction between vortices and free surface that are dependent from three-dimensional features of the flow.

6 Results and discussion

Figure 6a–h shows a selected sequence of snapshots of the free surface profile for Test #22 of Table 1, namely $KC = 1.54$ with $y^*/a = -3$, at non-dimensional time instants $t/T = j/8$, for $j = 0, \ldots, 7$. Experimental data from Contento and Codiglia [11] are reported with symbols. The corresponding dynamic pressure at the cylinder surface is shown on the right side. Both free surface elevation and pressure are actually averaged at the corresponding time t/T over four selected periods. The agreement can be considered respectable in terms of magnitudes and synchronism in all cases simulated.

The physics of this geometrically simple problem is characterized by the non-linear behavior of the free surface, by viscous effects in the near-body region, and appears very rich. Thus, the results are organized in three sections: wave transformation, flow field in the near region, and loads; each one is then subdivided in additional subsections for a detailed discussion.

6.1 Wave transformation

6.1.1 Energy transfer to super-harmonics

In this section, the wave transformation is investigated mainly in the frequency domain, essentially confirming (also quantitatively in comparable cases) the results obtained by Grue [14] on the amount of energy transferred to high order harmonics. Furthermore, it is shown that viscous effects on the free surface are still modest. This ensured the applicability of the methods that produced the reference literature within inviscid approaches.

Figure 7 shows the first η^I to the fifth η^V non-dimensional harmonic components of the free surface elevation vs x/a, for $y^*/a = -2$ and for KC, respectively, 0.40, 0.80, and 1.54. As a further comparison, an ideally inviscid flow with free slip condition at the cylinder wall is here simulated, actually resolving Euler equation, to evidence the effect of viscosity on the free surface.

In all cases, there is a clear growth of η^{II} and η^{III} on the lee side of the cylinder, starting from $x/a = -1$ approximately. At $KC = 1.54$, the amplitudes of η^{II} and η^{III} with viscous flow become almost constant with x/a, whereas they show a remarkable modulation with x/a for the lowest $KC = 0.40$.

As expected, the differences between viscous and inviscid flow become more pronounced with increasing KC, but still, they are not that large as those of the related pressures and forces (Sect. 6.3). As an example, Fig. 8 shows the time traces and the corresponding amplitude spectrum of the viscous and inviscid wave elevation at $x/a = 0$. In

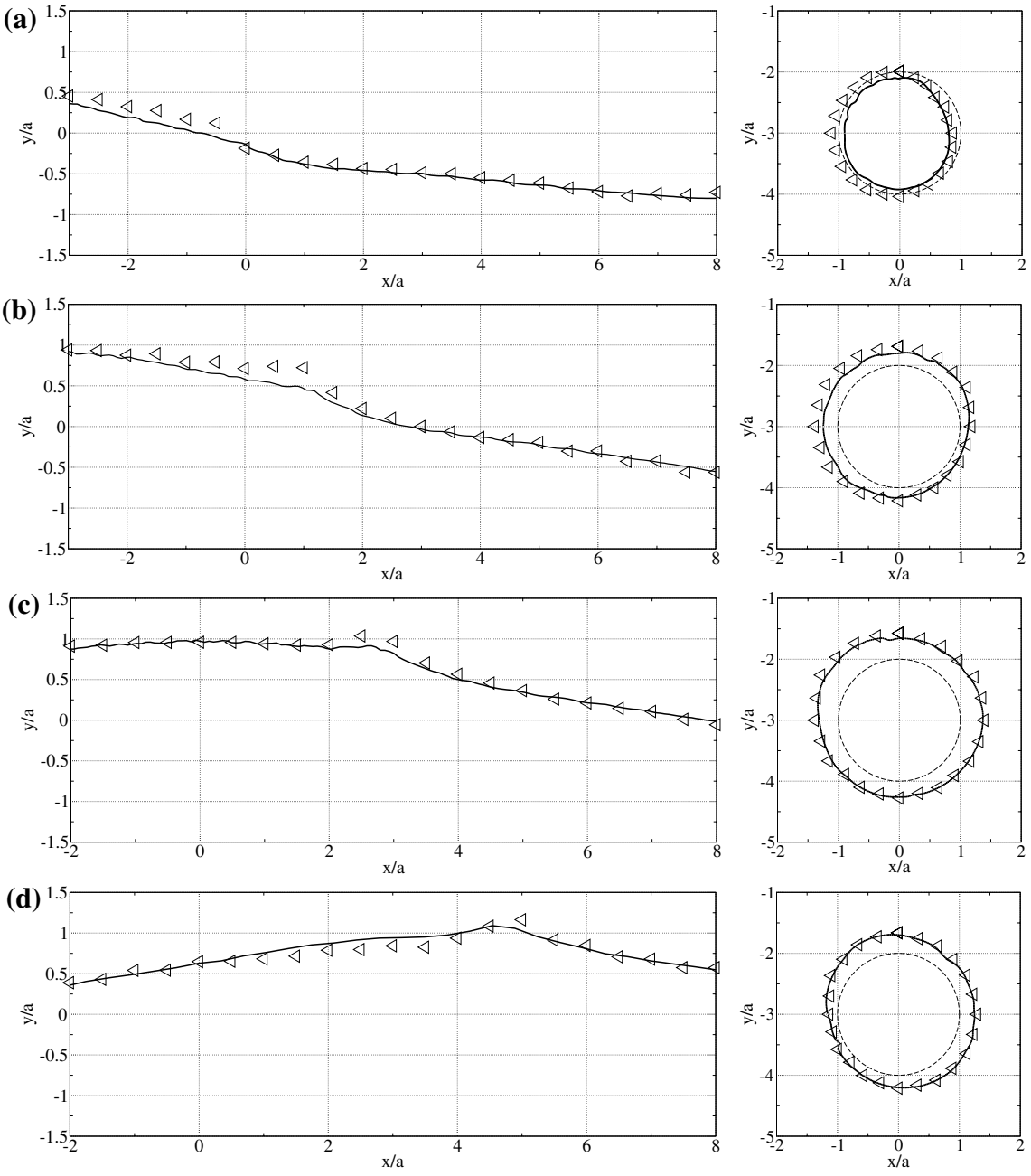

Fig. 6 Non-dimensional free surface elevation (*left*) and pressure at the cylinder surface (*right*): $KC = 1.54$; $y^*/a = -3$; **a** $t/T = 0/8$, **b** $t/T = 1/8$, **c** $t/T = 2/8$;⋯;1 radius corresponds to 1 kPa; ◁ = exp. [11], *solid line* present numerical

the viscous simulations, there is just a slightly pronounced high-frequency oscillation for $KC = 1.54$.

For $KC = 1.54$ and $y^*/a = -2$, waves break, regardless of the viscous or inviscid flow. The presence of the viscosity induces a vorticity structure detaching periodically at the cylinder upper part [22, 29], with onset from $\theta > 270°$ approximatively, and occurring almost simultaneously with the wave breaking. Figure 9a, b shows the instantaneous and synchronous vorticity field in the inviscid (a) and viscous (b) flow simulation, respectively. The vortices detached at the Northern part of the cylinder as in Fig. 9b produce no macroscopic effects on the free surface behavior in terms, at least, of the first three harmonic amplitudes (see Fig. 7). However, in the proximity of the cylinder and even in the inviscid approach, the free surface is at least affected by vorticity initialized by the wave overturning shear (Fig. 9a). However, it is difficult to define details on the vortex connection mechanism with the free surface,

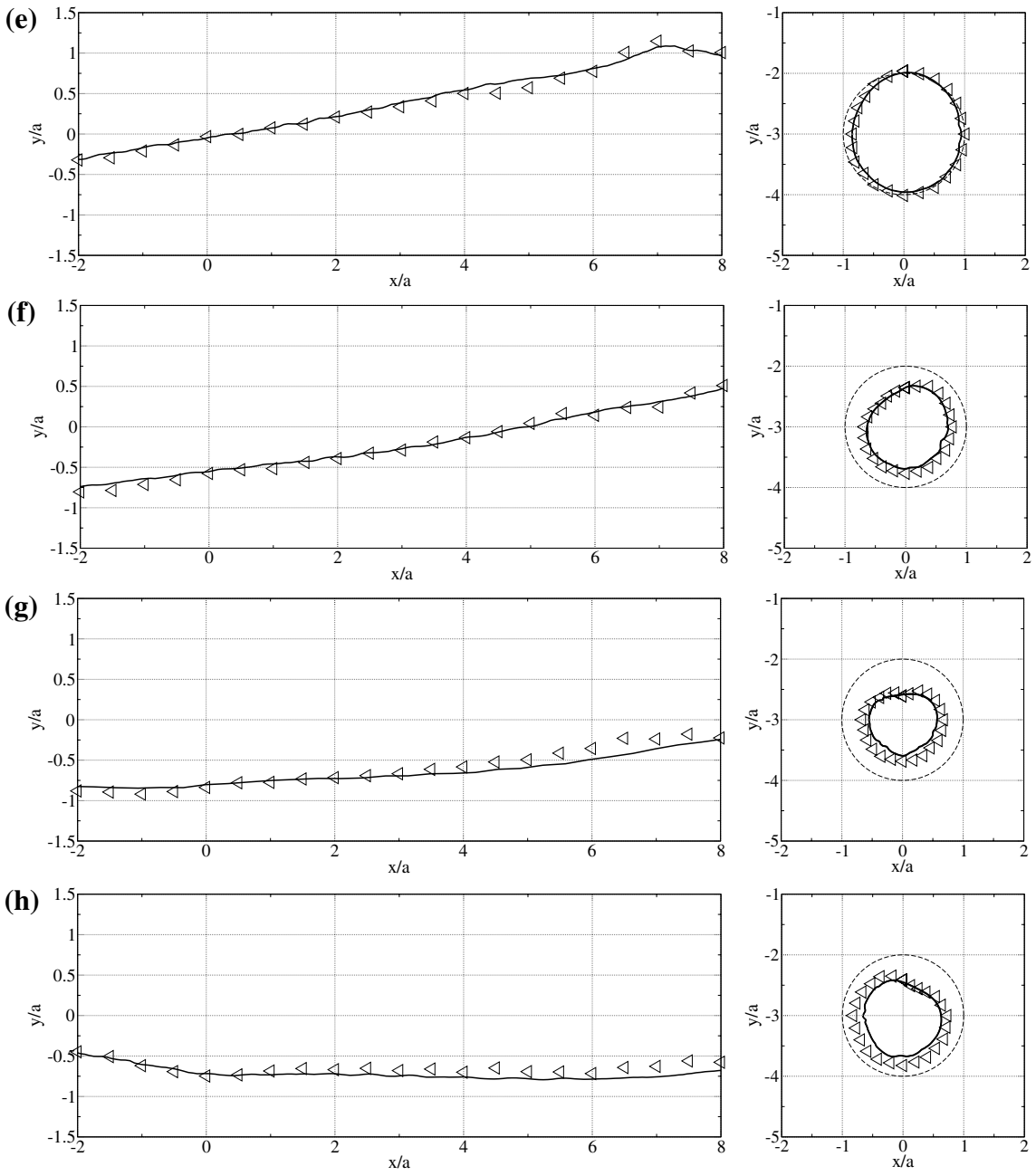

Fig. 6 (continued)

since the simulations, even if well resolved, are conducted in 2D approximation and the vorticity is transported towards the free surface only by the diffusion term of Eq. 3 and in absence of vortex stretching [43].

Harmonics higher than the third are systematically found in the simulations (Fig. 7), the max magnitude of the fourth and fifth being comparable to the third. They are found in a bounded region around the cylinder for low KC or spread downstream for higher KC, both in viscous and inviscid flow simulations with extremely similar longitudinal distribution and amplitudes.

Finally, Fig. 10 shows a summary of the amplitude of the first $\bar{\eta}^I$, second $\bar{\eta}^{II}$, and third $\bar{\eta}^{III}$ Fourier components of the free surface elevation vs KC, non-dimensionalized by the incident wave amplitude. Following Grue [14], $\bar{\eta}^I$, $\bar{\eta}^{II}$ and third $\bar{\eta}^{III}$ are here the space averages of each harmonic at the lee side of the cylinder axis, in the present case for $1 \leq x/a \leq 8.5$.

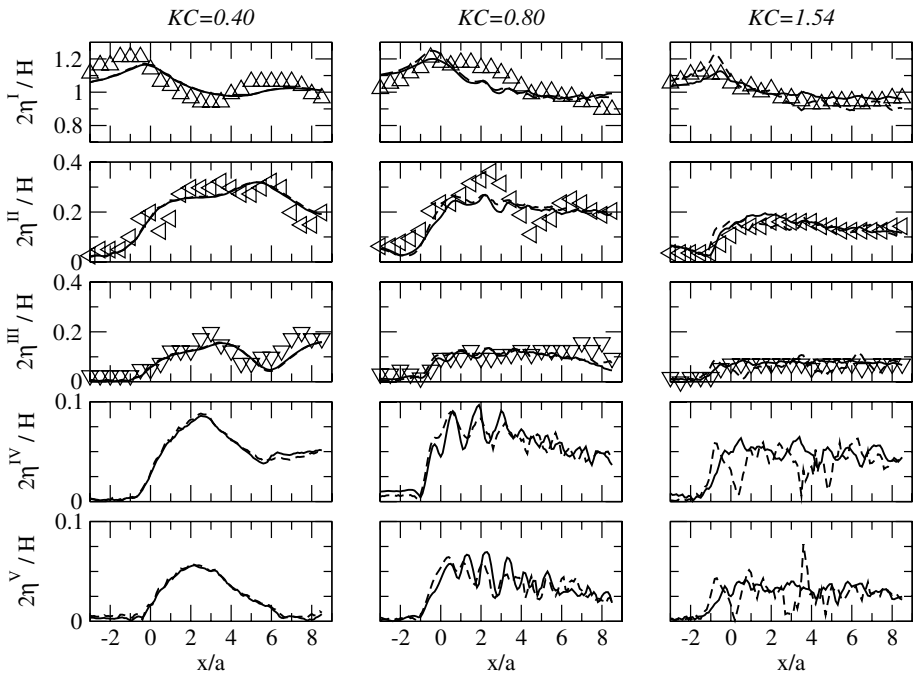

Fig. 7 Non-dimensional Fourier components η^I to η^V (from *top* to *bottom*) of the free surface elevation vs x/a, for $y^*/a = -2$, $KC = 0.40$ (*left*), $KC = 0.80$ (*center*), and $KC = 1.54$ (*right*). *Symbols* experimental [11], *solid line* present numerical (viscous), *dashed line* present numerical (inviscid)

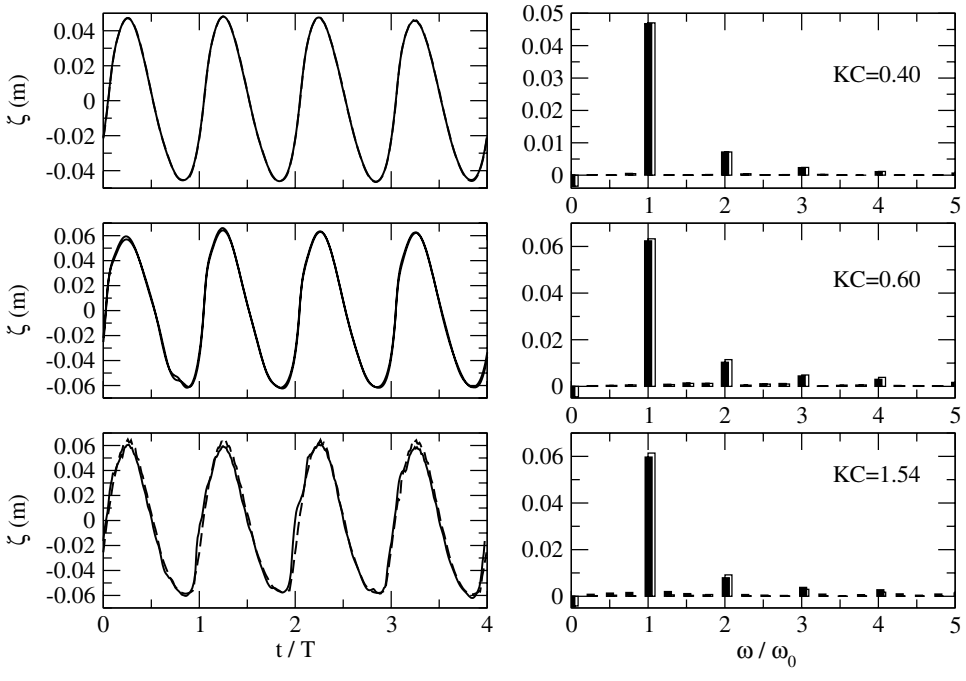

Fig. 8 Wave elevation for $y^*/a = -2$ at $x/a = 0$ with cylinder present (*left*) and corresponding amplitude spectrum (*right*). $KC = 0.40$, $KC = 0.80$ and $KC = 1.54$ (from *top* to *bottom*). *Solid line* or *full bar* = viscous, *dashed line* or *empty bar* = inviscid

In the upper part of the KC range, in the case $y^*/a = -2$, the low submergence of the cylinder induces a large breaking and a related evident reduction of the first harmonic $\bar{\eta}^I$.

Furthermore, for every submergence, at low KC, there is an almost linear rapid growth of both $\bar{\eta}^{II}/(H/2)$ and $\bar{\eta}^{III}/(H/2)$ with KC. This second-order behavior is less steep if the cylinder depth is increased. At high KC values, both $\bar{\eta}^{II}/(H/2)$ and $\bar{\eta}^{III}/(H/2)$ exhibit a kind of saturation. This effect has been observed, among others, by Grue [14] for the second harmonic; his experiments were performed for shallower cylinders, his deepest condition being our shallowest. In that case, the saturation phenomenon of the higher harmonic components was observed systematically even for very low KC numbers, $KC < 0.4$. Grue [14] also showed that the KC value at which this saturation effect starts, increases with the increasing depth of the cylinder. Both experiments from Contento and Codiglia [11] and the present simulations show that for $KC < 0.80$, this second

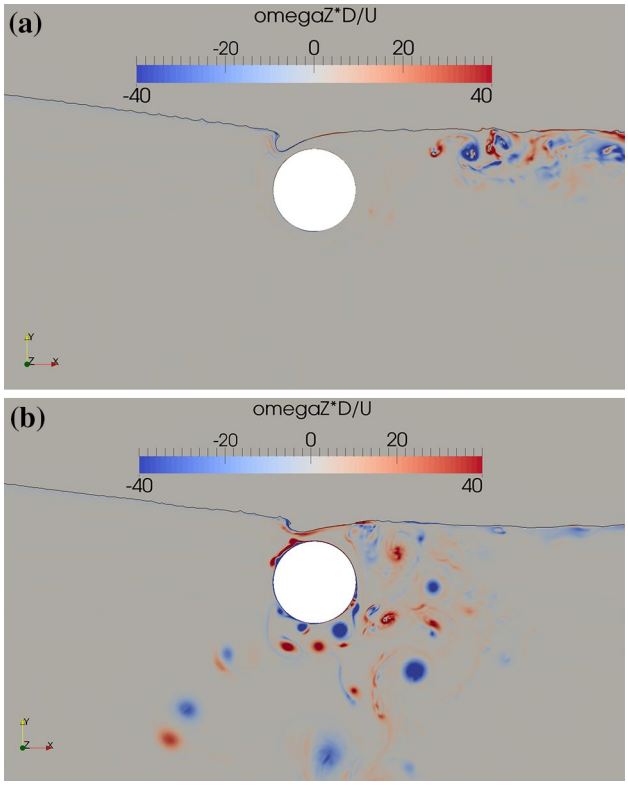

Fig. 9 Free surface profile and non-dimensional vorticity field for inviscid (**a**) and viscous (**b**) flow simulations at $t/T \simeq 0.9$, $KC = 1.54$, and $y^*/a = -2$. The vorticity present in the inviscid flow simulation is generated by the overturning of waves

harmonic can be as large as at least 4 times the second-order component of the incident wave in a Stokes' third-order expansion.

In the upper most part of the investigated *KC* range, the experimental values are quite spread. This result is difficult to read. The present simulations suggest that this effect is related to the detachment of vortexes from the cylinder surface and to their interaction in complex patterns that was impossible to detect with the available laboratory setup.

6.1.2 Wave reflection

Since the pioneering work of Dean [12], it has been shown that there is no wave reflection from the cylinder in the frame of linear potential theory. Schonberg and Chaplin [35] reconsidered the problem still within the inviscid flow scenario and suggested that the reflected waves behave at fourth order in the wave steepness, i.e., the reflection coefficient behaves as $(kA)^3$, where A is the incident wave amplitude. The results were assessed for both deep and shallow waters.

In this subsection, the reflection coefficient is computed according to linear theory for the full set of simulated cases:

$$CR^I = \frac{H_R^I}{H} = \frac{A_{\max} - A_{\min}}{A_{\max} + A_{\min}}. \tag{9}$$

The region considered is $-2.5\lambda < x < -0.5\lambda$. The amplitudes $A_{\max}$, $A_{\min}$ above are the max and min of the first harmonic of the wave elevation, respectively. They are

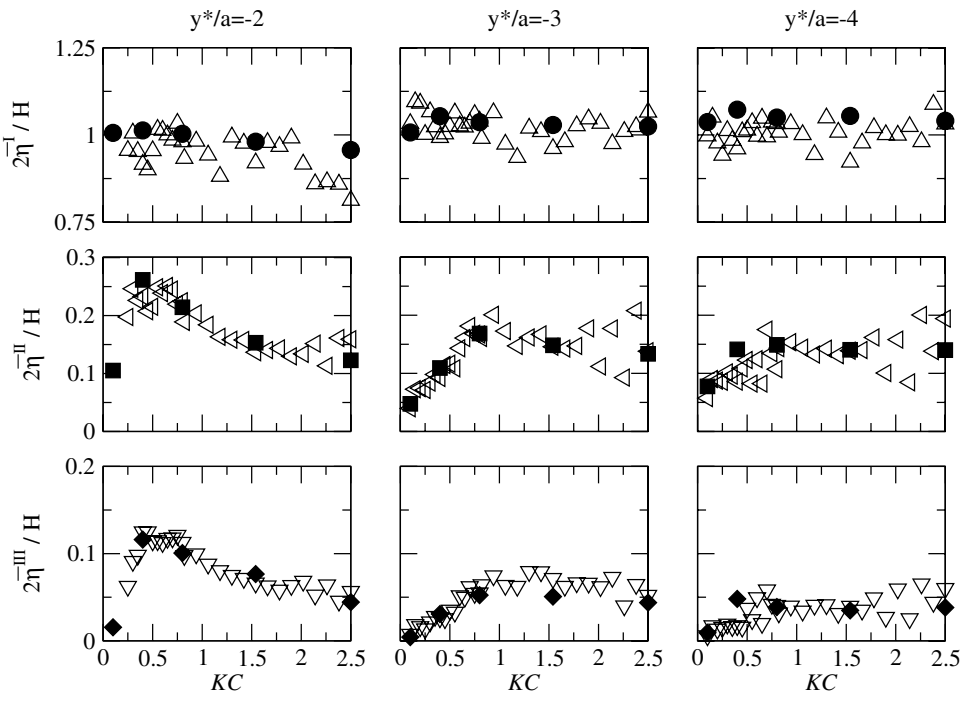

Fig. 10 Non-dimensional Fourier components η^I, η^{II}, and η^{III} (from *top* to *bottom*) of the free surface elevation vs *KC*, averaged at the lee side of the cylinder in the range $1 \le x/a \le 8.5$. $y^*/a = -2$ (*left*); $y^*/a = -3$ (*center*); $y^*/a = -4$ (*right*). *Empty triangles* = exp.; *solid symbols* = present num

expected to occur at two adjacent longitudinal positions with a distance $\lambda/4$ between them. This is shown in Fig. 11, for a sample case $KC = 0.10, y^*/a = -3$.

The summary of the results obtained for CR^I is presented in Fig. 12. Data are related to the cases given in Table 1, enriched, for this purpose only, with other cases at intermediate KC numbers. The maximum value achieved is $\approx 2.6\%$. Consistently with the discussion by Schonberg and Chaplin [35], the reflection coefficient CR^I is here plotted against $(kA)^3$. In Fig. 12, the best fit line is given as

$$CR^I = a + b \cdot (kA)^3 \tag{10}$$

with $a = 0.0076$ and $b = 2.04326$. The data are rather scattered, due to the extreme sensitivity of Eq. 9 to the fluctuations of A_{max} and A_{min} in space and to the heterogeneous set of data with different cylinder submergences. However, the general trend at third order of CR of the first harmonic of the free surface elevation seems reasonably confirmed by the simulations as a good ensemble approximation. Schonberg and Chaplin [35] obtained a much higher b in the different conditions of shallower cylinder, unique diffraction parameter, and inviscid flow approximation, and thus, the comparison is not straightforward.

6.2 Flow field in the near region

6.2.1 Vorticity and main vortexes detachment

The present simulations reveal large-scale detached eddies in the 2D flow. The task is here to identify the vortex shedding patterns and possibly to correlate the detachment region to the pressure distribution at the cylinder surface. In this context, the work of Otsuka and Ikeda [30] is of reference. With reference to the experimental patterns in Fig. 4b of the mentioned paper, large-scale counter-clockwise eddies have been observed to separate from the cylinder

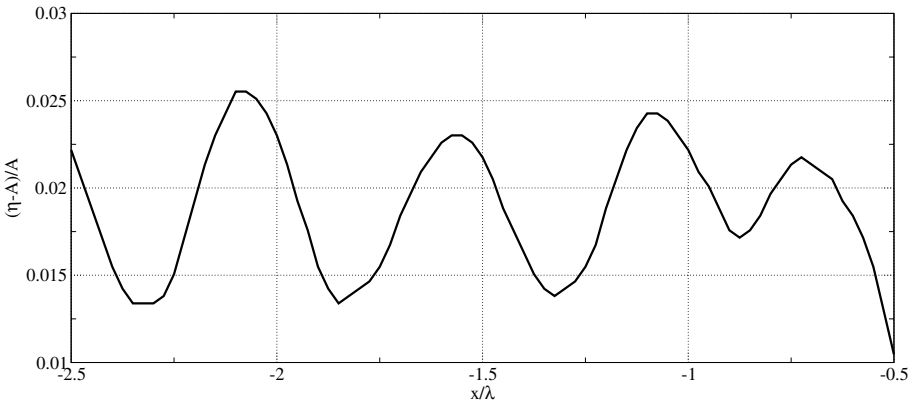

Fig. 11 Non-dimensional variation of the first harmonic of the wave elevation η^I on the weather side of the cylinder. $KC = 0.10$, $y^*/a = -3$

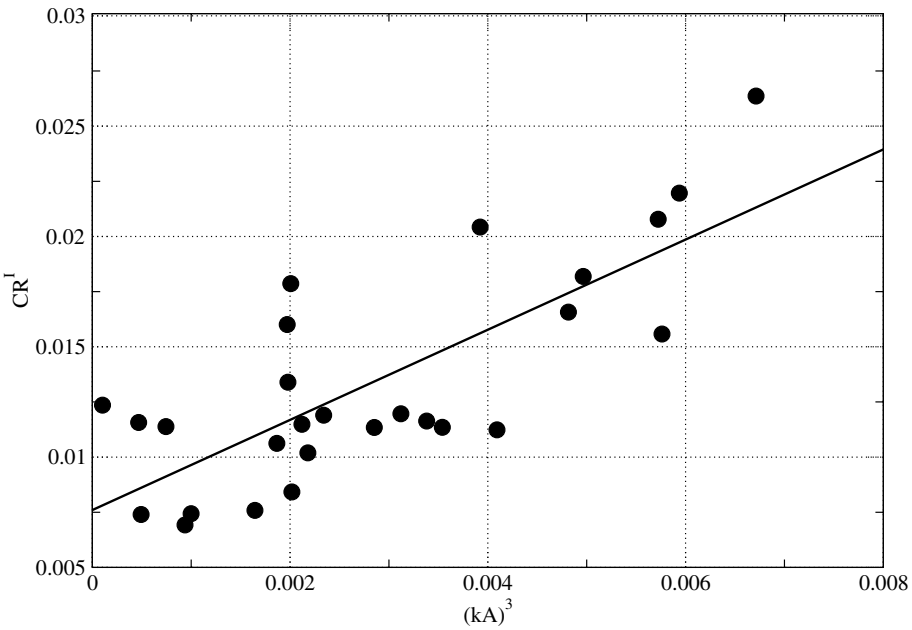

Fig. 12 Reflection coefficient vs $(kA)^3$ from the simulations and best fit line

twice per wave period. Then, a sequence of induced opposite (clockwise) vortices rolls up and keep rotating around the cylinder.

This mechanism has been recognized to occur at the North side of the submerged cylinder in the presented numerical simulations. At the reference time $t/T \approx 0$, i.e., at the unperturbed wave up-crossing above the cylinder axis, as shown in Fig. 13a, a pair of counter-rotating eddies (1 and 2) is generated at the upper part of the cylinder. They start moving around the cylinder in clockwise sense. Vortex 1 is detached first, while, for $0 < t/T < 1/4$ approximately, before the wave crest reaches the cylinder axis, the clockwise vortex 2 is rolled up in a prolonged shape by the dominant flow that now is horizontal at the cylinder axis. The counter-clockwise rotating vortex is shed at $\theta \approx 30\,°$ –50 °. The prolonged clockwise vortex is shed later on before reaching $\theta \approx 120\,°$–150 ° as represented in Fig. 13b. Two other vortices (3 and 4) are indexed in the figures: they

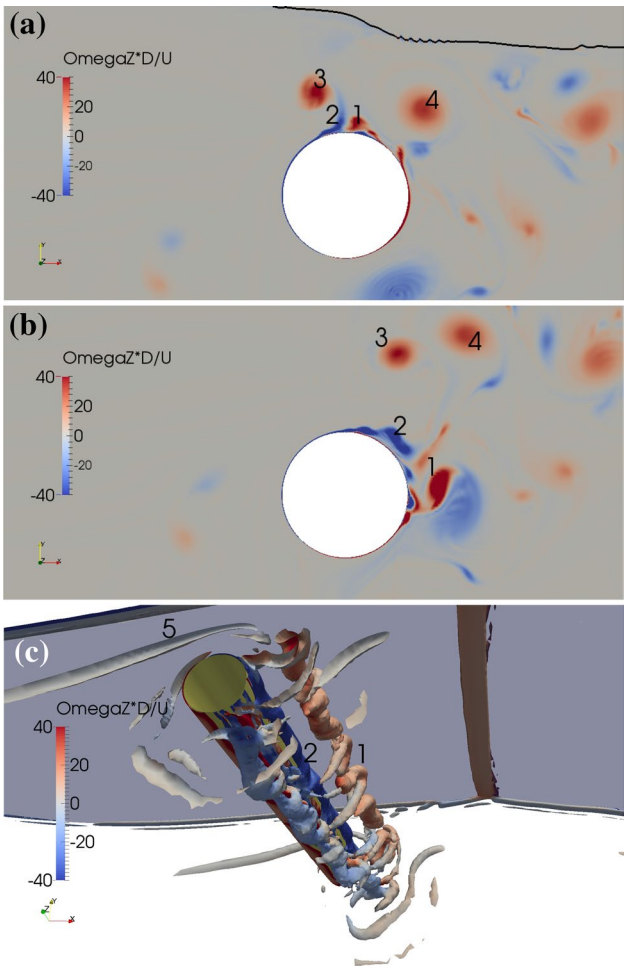

Fig. 13 Snapshots of the non-dimensional vorticity field at $KC = 2.50$, $y^*/a = -3$; **a** $t/T = 0$, **b**, **c** $t/T \simeq 0.2$

are the results of previously occurred detachments and still remaining in the proximity of the cylinder.

The detachment mechanism is now developing again from South–West to occur again in the South of the cylinder during the single-wave period selected. In the numerical experiments here produced, it is observed that this second occurrence is frequently polluted by the interaction with previously detached vortices.

On average, an almost steady clockwise circulation is thus originated around the cylinder.

This mechanism is present at all submergences and for all *KC*, with increasing complexity with increasing *KC*. Even the occurrence of a breaking wave event does not turns this effect off, as shown in Fig. 25a, b in Lupieri and Contento [22].

Test # 30 for $y^*/a = -3$ has been conducted considering a 3D domain too, in the RANS approach. For shake of clarity, in this case, vortices have been recognized and limited in space according to the criterion:

$$Q = \frac{1}{2}[|\Omega|^2 - |S|^2] > 0$$

where S is the strain rate tensor and Ω the vorticity tensor as described by Haller [16], then the normalized Ω_z vorticity component is represented in Fig. 13c with $Q = 1$. It is evidenced that, also in this case, the detachment occurs with a pattern similar to the one described for the 2D case: the counter-clockwise first (1 in figure) and then the eddy rolling (2 in figure), meaning that the bulk mechanism is still mainly driven by the wave periodicity and surface proximity. Furthermore, in the same figure, zone 5, the (relatively mild) vorticity associated with the boundary layer at lateral bulkheads is evidenced, whose influence has been visualized also during the experimental sessions.

Figure 14a, b shows the time traces of the non-dimensional vorticity and pressure at a very small distance from the cylinder surface, at $\theta = 0\,°$ and $\theta = 60\,°$ for the sample case $KC = 0.80$ and $y^*/a = -2$. At $\theta = 0\,°$, the quasi-impulsive behavior of the vorticity around $t/T = 0 + i$, for any i, is well evidenced and witnesses the passage of the pair of eddies, the positive (counter-clockwise) vortex first, the negative immediately after, with a greater magnitude and prolonged persistence of the latter. At $\theta = 60\,°$, the impulsive behavior has a reduced magnitude with a larger number of high-frequency oscillations. Both positions θ show an evident relation to pressure pulses found at the cylinder surface (lower plots of Fig. 14a, b and see also Sect. 6.3.2).

6.2.2 *Circulation around the cylinder*

The circulation reads as a measure of vorticity intensity in the flow, here computed within a path encircling the

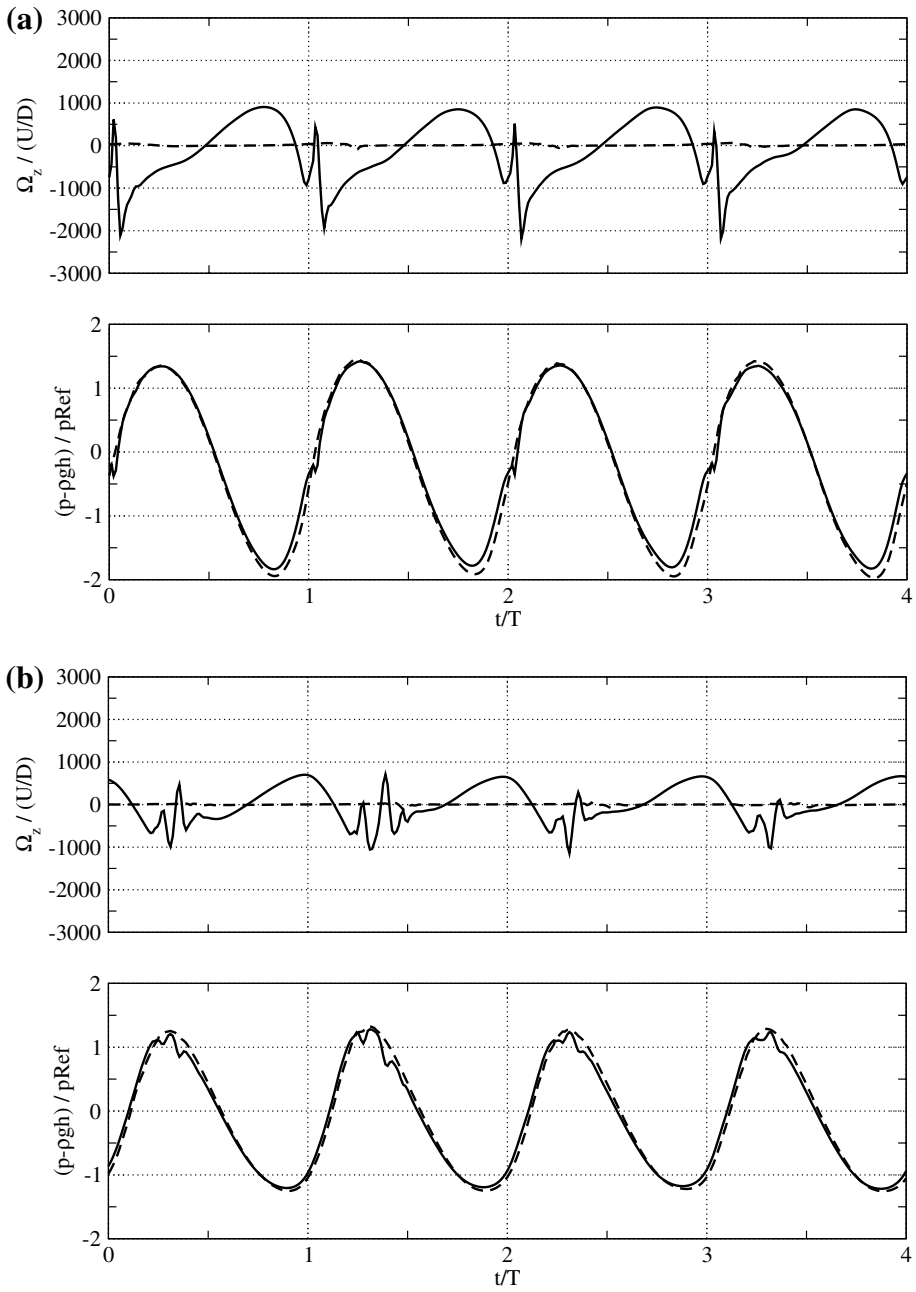

Fig. 14 Non-dimensional vorticity and pressure at **a** $\theta = 0\,^\circ$ and **b** $\theta = 60\,^\circ$ at a very small distance from the cylinder surface. $KC = 0.80$, $y^*/a = -2$. *Solid line* viscous flow, *dashed line* inviscid flow

cylinder at a increasing distance from the wall. Figure 15 shows the non-dimensional average circulation $\Gamma/(aU)$ for different KC values. The curves belong to the case $y^*/a = -4$, i.e., far from strong free surface proximity effects as wave breaking. Consistently with the analysis of Stansby and Smith [37], the maximum circulation occurs at a distance that increases with KC, while the shape of the radial distribution of $\Gamma/(aU)$ can be related to the vorticity structures present in the flow, at increasing distance with increasing KC.

At small KC numbers, say $KC < 0.80$, the flow is almost irrotational not far from the boundary layer and the bulk of the circulation is bounded in a narrow region. It vanishes at a distance $\approx 20\%$ of the radius for $KC = 0.40$, and ≈ 1 radius for $KC = 0.80$. At higher KC numbers, the flow departs from its irrotational condition: the population and intensity of the vorticity structures detached from the cylinder are observed to increase; after the depart from the cylinder, their intensity progressively decreases for subsequent interactions with other vortices or with the free surface.

On average, a steady clockwise circulation originated by the vortex detachment (after Otsuka and Ikeda [30]) is detected around the cylinder, as shown in Fig. 16. Vectors are obtained by sampling the velocity field along 12

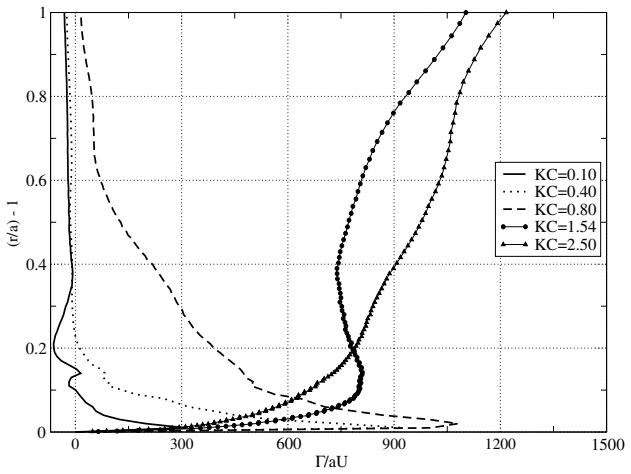

Fig. 15 Non-dimensional circulation Γ vs non-dimensional radial distance from cylinder surface

selected directions branching off radially from the cylinder and averaging over the time window $0 \leq t/T < 4$. On the East and South–East side of the cylinder, strong gradients of the velocity profiles are clearly visible. This relates once again to the presence of the complex vorticity structures of both signs, detaching and interacting in the boundary layer proximity.

6.3 Loads on the cylinder

6.3.1 Pressure field at the cylinder surface

This section is mainly devoted to the comparison between the experimental and numerical results and to highlight specific features not available from the experiments.

Figure 17a–e shows the non-dimensional Fourier components $p^j(\theta, KC, y^*/a)$ of the pressure at the cylinder surface, up to the third harmonic, as a function of the submergence y^*/a, of the azimuth θ and of KC, both experimental [11] and present numerical results. The reference pressure $pRef$ is assumed as the amplitude of the undisturbed dynamic pressure at the cylinder axis from the linear wave model, i.e., $pRef = KC\frac{\rho g D}{2\pi}$.

Mostly for $KC = 0.10$, but, in general, for $KC < 0.80$, the third harmonic of the measurements is extremely small and almost constant with θ, due to sensitivity limits of the transducers. For this reason, the comparison of the third harmonic is not straightforward in this KC range. In the other cases, the simulations confirm closely what had been observed in the experiments.

As for $p^I(\theta, KC, y^*/a)$, for $KC < 0.80$, the distribution is almost symmetric with respect to $\theta = 180\,°$. For a selected KC number, the positive peaks at $\theta \approx 0\,°$ seem insensitive to the cylinder depth, whereas the negative peaks are more

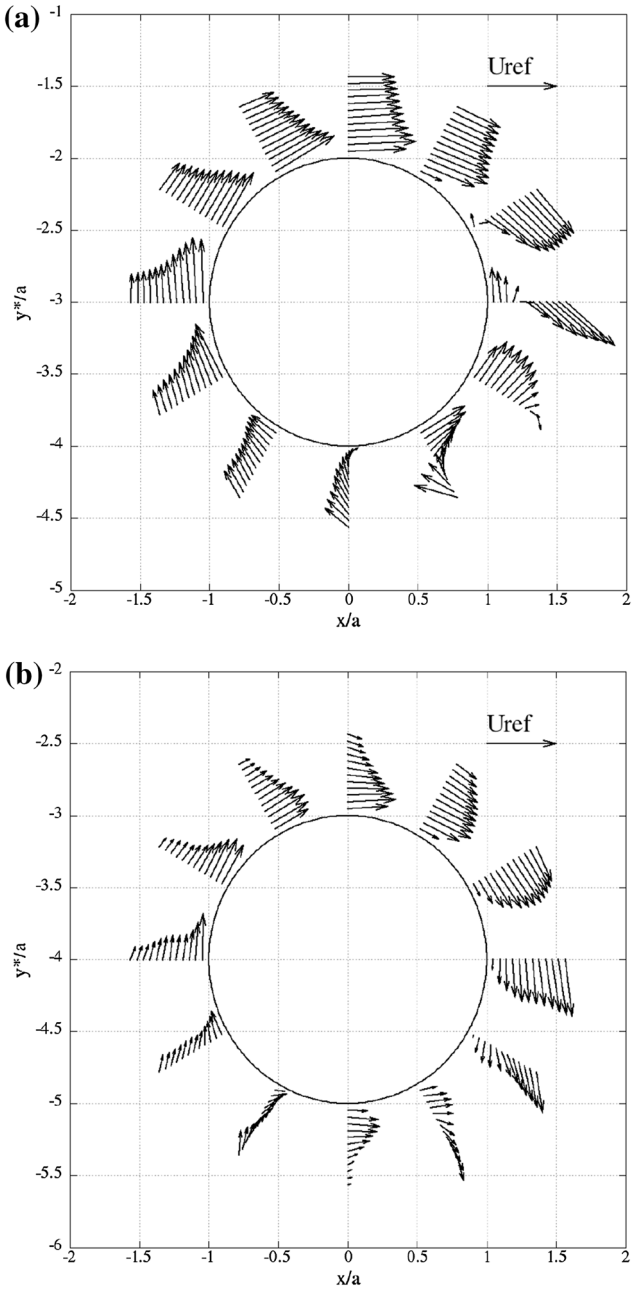

Fig. 16 Non-dimensional averaged velocity field (under-sampled for graphics purposes) around the cylinder, $KC = 2.50$, $U_{\text{ref}} = KC \cdot D/T$, **a** $y^*/a = -3$, **b** $y^*/a = -4$

pronounced for a shallower cylinder. The strong variation of $p^I(\theta, KC, y^*/a)$ with θ then flattens itself progressively with increasing KC, both in the experimental and numerical results, and the symmetrical distribution is progressively lost.

As for $p^{II}(\theta, KC, y^*/a)$, with reference to the experimental results given in Fig. 5 of Contento and Codiglia [11] and with specific reference to the plots (a.2, b.2, c.2), in the case $y^*/a = -2$ (a.2), there is a large peak of

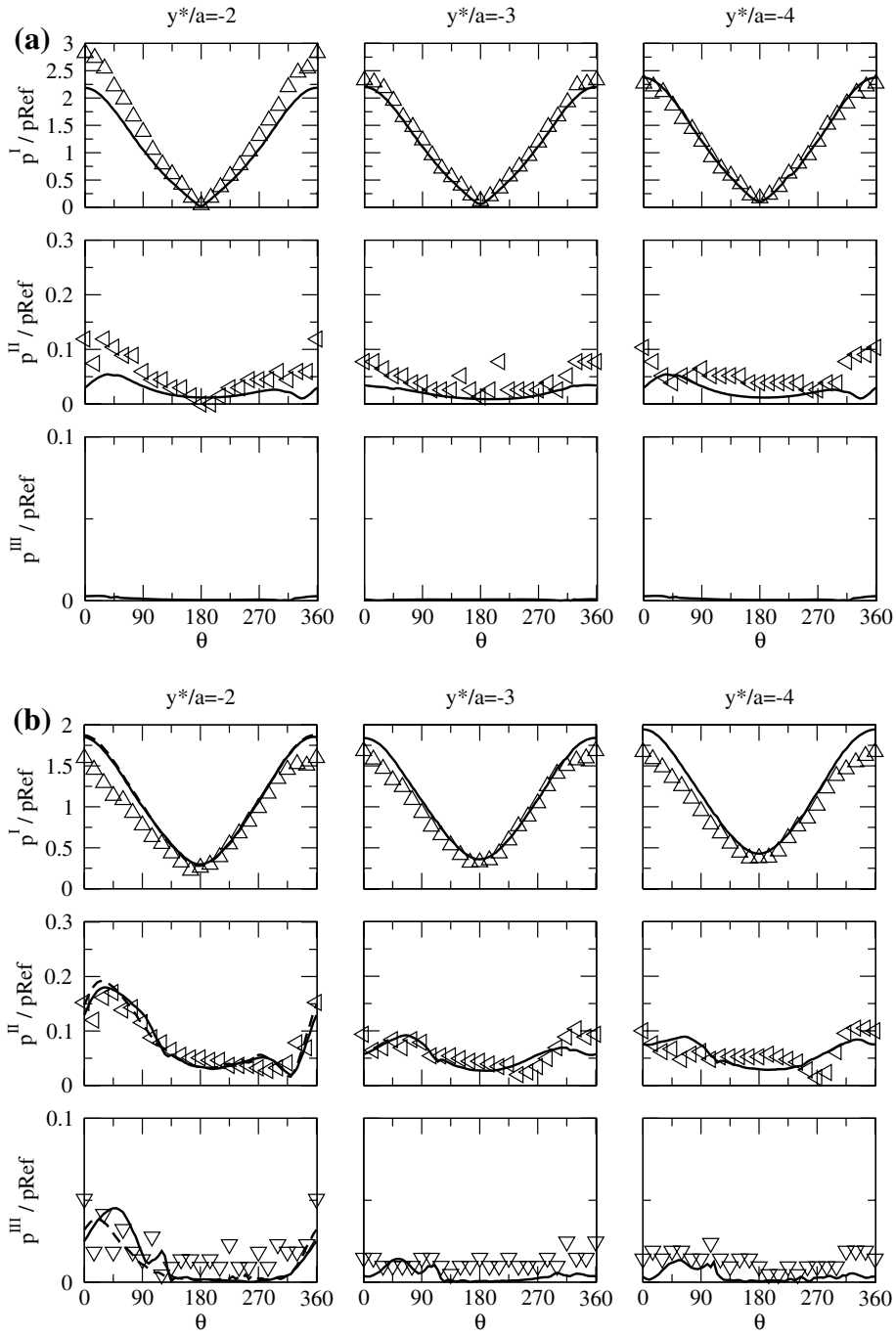

Fig. 17 Non-dimensional first p^I, second p^{II}, and third p^{III} Fourier components of the pressure at the cylinder surface vs θ. **a** $KC = 0.10$; **b** $KC = 0.40$; **c** $KC = 0.80$; **d** $KC = 1.54$; **e** $KC = 2.50$. *Symbols* exp, *solid line* numerical (viscous), *dashed line* numerical (inviscid)

the second harmonic component for $0.20 < KC < 0.80$, up to $\approx 25\%$ of $p^I(\theta, KC, y^*/a)$. This large amplitude component shows its max values in the range $0° < \theta < 90°$. p^{II} then reduces its values with increasing KC. This is consistent with the expected diffraction effect of the second-order locked waves in the specified range, mostly in the case $y^*/a = -2$. The case $KC = 0.1$ evidences the largest differences between numerics and experiments on p^{II} at all y^*/a. This is again due also to sensitivity limits of the transducers and the problem still remains under investigation. For $y^*/a = -2$, at all KC, the numerics exhibits, clearer than the experiments, a second minimum for p^{II} around $\theta = 315°$–$330°$, due to the interaction with the free surface. This minimum is no longer visible for deeper cylinders.

As for $p^{III}(\theta, KC, y^*/a)$, considering the extremely low values of this component and the difficulties in the measurements, the general behavior is captured and so the overall local magnitudes but still the numerical simulations show many deep local hollows, not always present in the

Fig. 17 (continued)

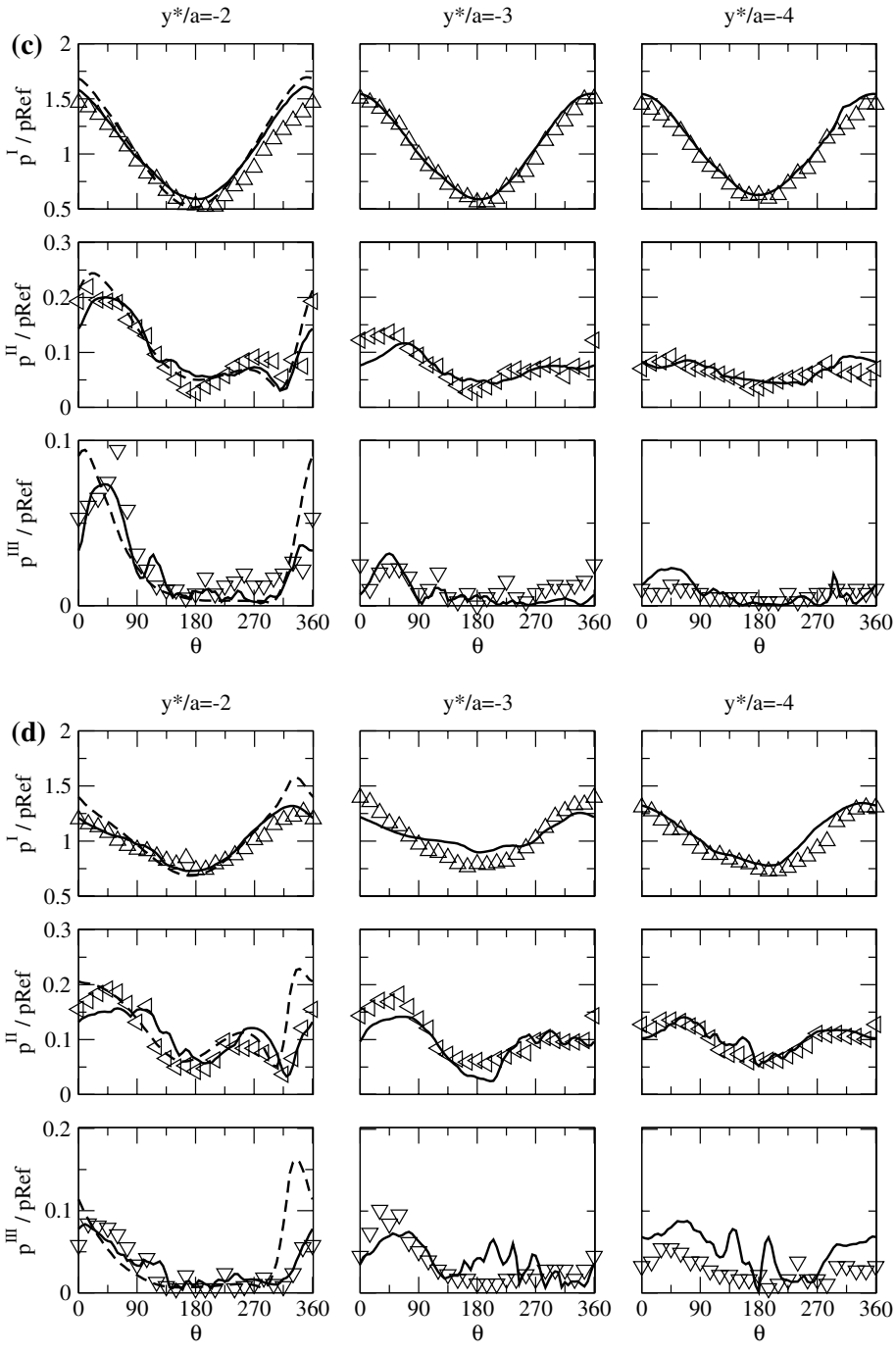

measurements, that are probably related to vortex detachment regions.

Should we continue with the analysis to higher harmonics, we would find non vanishing amplitudes, mostly in specified regions on the cylinder surface. Looking at the time series of the pressure, for instance $KC = 0.80$, $y^*/a = -2$, $\theta = 0\,°$, or $\theta = 60\,°$ (Fig. 14a, b lower plots), there are evident repeated pulses of the pressure in the viscous flow simulation (solid line), strongly related to the vorticity jumps and to the vortex detachment at the same location. They occur in a limited region and appear at specific t/T. The dashed lines in the previous figures show the inviscid flow solution and no symptoms of pressure pulses are found.

Finally, it is interesting to look further at the effect induced by viscosity on the pressure field. To this purpose, in Fig. 17, the dashed lines for the cases $KC = 0.40, 0.80, 1.54$ and $y^*/a = -2$ show the inviscid flow solution. In particular, for $KC = 1.54$, there is a clear overestimation of the inviscid flow in the region

Fig. 17 (continued)

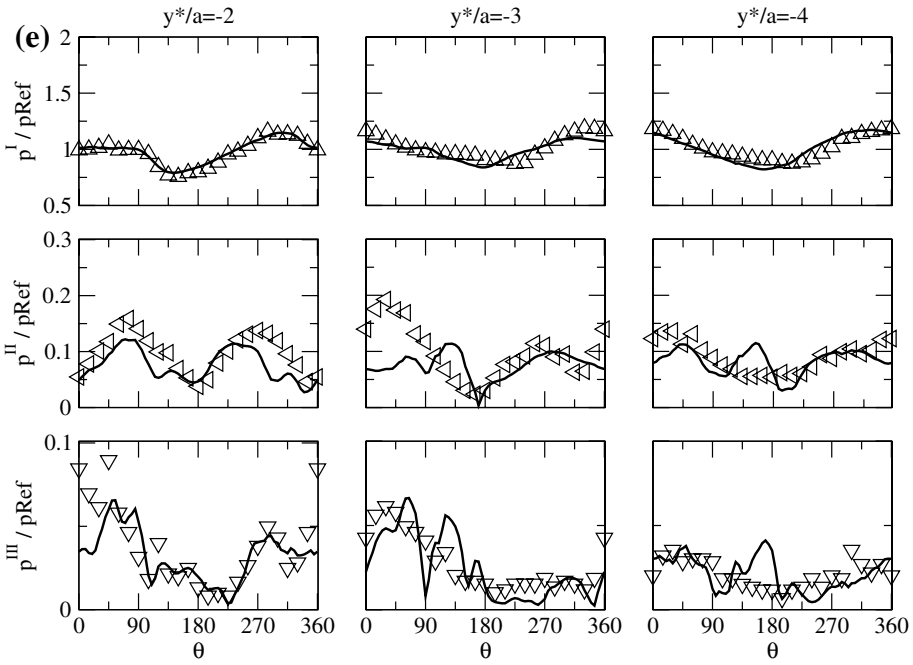

$270° < \theta < 360°$ for both p^{II} and p^{III}. This is associated with the region of development of the pair of vortexes discussed in Sect. 6.2.1.

6.3.2 *Forces on the cylinder*

Figure 18a–c shows the non-dimensional amplitude of the first F^{I}, second F^{II}, and third F^{III} Fourier harmonics of the horizontal and vertical components of the force vs *KC*, each plot refers to a different submergence y^*/a. Concerning the

Fig. 18 Non-dimensional Fourier components of the forces on the cylinder vs *KC*. **a** $y^*/a = -2$; **b** $y^*/a = -3$; **c** $y^*/a = -4$. F^{I}: *triangle* exp and *filled circle* = num; F^{II}: *left arrow head* exp and *filled square* numerical (viscous); F^{III} : *downward triangle* exp and *filled diamond* = numerical (viscous)

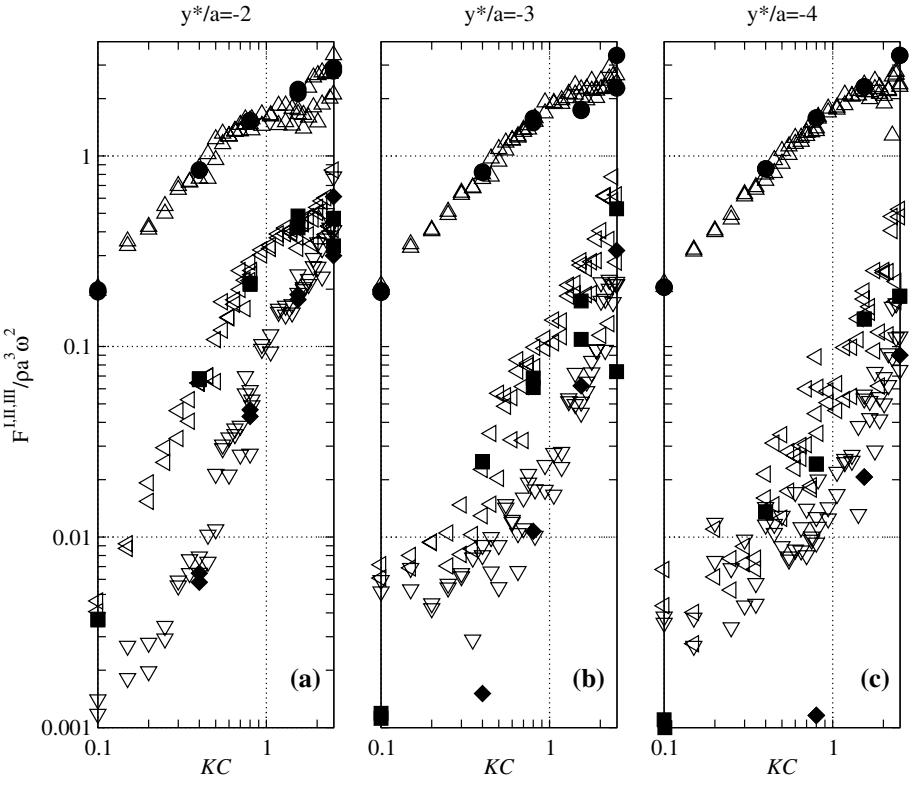

first two harmonic components, the comparison between present numerical results and experiments can be considered extremely satisfactory. As for the third harmonic at the lowest *KC* numbers and deepest cylinder, sensitivity limits of the pressure transducers [11] and the related pressure integrals make the comparison questionable. Forces are indeed obtained as the integral of the pressure at the cylinder, and therefore, the results can reflect the properties already discussed for the pressure field.

In accordance to the results of Chaplin [2] and Contento and Codiglia [11], the first Fourier component F^I is almost insensitive to the submergence of the cylinder. Some small oscillations appear for $KC \geq 1.5$ with $y^*/a = -2$, where the proximity of the free surface and occurrence of separation lead to a departure from the pure inertia term.

The second harmonic F^{II} shows an evident dependence on the cylinder submergence. For the case at $KC = 2.50$ with $y^*/a = -2$, the numerics exhibits small deviations, probably related to eddies detachment that was not captured by the experimental pressure gauges. Moreover, at $KC = 0.1$ and $y^*/a = -3, -4$, the numerical results of F^{II} show an evident underestimation, again also related to sensitivity limits of the transducers.

7 Concluding remarks

This study has been focused on three main aspects of the interaction of a weakly submerged horizontal circular with regular waves: wave transformation, flow field in the near region, and loads on the cylinder. The numerical simulations conducted have given a good representation of the experimental data and have allowed a closer insight in flow details not available from the experiments.

As for the wave transformation, the simulations have confirmed the strong energy transfer from the first to higher frequencies induced on the lee side of the cylinder. In particular, harmonics higher than the third and with non-negligible amplitude have been found. Supported by the measurements, the simulations have shown that the second harmonic can be as high as 25% of the first and that both second and third harmonics exhibit a saturation process, for increasing *KC*. The additional simulations conducted within the inviscid fluid hypothesis have shown that up to the third harmonic or even higher, the differences with the viscous flow simulations are not relevant in the free surface representation. Small amplitude reflected waves from the cylinder have been observed at the first harmonic with a related reflection coefficient that behaves non-linearly at third order in the incident wave slope.

As for the flow field in the near region, the onset, development, and detachment of counter-rotating eddies that lead to an average steady streaming have been analyzed and related to pressure loads, in particular to pressure pulses on the upper part of the cylinder surface. These pulses are not present in inviscid flow simulations.

Both simulations and experiments show that the first Fourier component of the global force exhibits a strongly non-linear behavior of viscous origin. This component (at the dominant wave period) is only weakly dependent on the cylinder submergence. On the contrary, the second and third Fourier components show a great variability with the submergence with a rapid growth as the cylinder approaches the free surface.

As a general final comment, the presented simulations have confirmed the results previously obtained experimentally and added hints on aspects that could not be investigated, as the vorticity patterns and the departure from irrotational regime relatively far from the cylinder at high *KC* numbers. Furthermore, they have evidenced the role of the viscosity in the representation of the free surface and in the flow field close to the cylinder. These two aspects can result crucial in the choice of suited numerical approaches.

An additional insight could be the focus on the locally turbulent flow at the breaking region, while a further study with shallower cylinders and higher diffraction parameter is in progress.

Acknowledgements The *Programma Attuativo Regionale* del Fondo per lo Sviluppo e la Coesione (PAR FSC 2007-2013) Linea d'Azione 3.1.2 is acknowledged for providing the financial support of the OpenViewSHIP Project.

References

1. Chaplin JR (1984) Mass transport around a horizontal cylinder beneath waves. J Fluid Mech 140:175–187
2. Chaplin JR (1984) Nonlinear forces on a horizontal cylinder beneath waves. J Fluid Mech 147:449–464
3. Chaplin JR (1988) Loading on a cylinder in uniform oscillatory flow: Part I—Planar oscillatory flow. Appl Ocean Res 10:120–128
4. Chaplin JR (1992) Orbital flow around a circular cylinder. Part 1. Steady streaming in non-uniform conditions. J Fluid Mech 237:395–411
5. Chaplin JR (1993) Orbital flow around a circular cylinder. Part 2. Attached flow at larger amplitudes. J Fluid Mech 246:397–418
6. Chaplin JR (2001) Non-Linear Wave Interactions with a Submerged Horizontal Cylinder. In: Proceedings of the Eleventh (2001) International Offshore and Polar Engineering Conference, vol III, pp 272–279
7. Chiu H (1973) Diffraction of water waves by a submerged circular cylinder. In: College of Engineering Rep. N A 73-4, University of California, Berkeley, CA
8. Clement A (1995) Coupling of two absorbing boundary conditions for 2d time-domain simulations of free surface gravity waves. J Computat Phys 126:139–151
9. Contento G (1995) A numerical wave tank for the free floating body problem. In: Proceedings of the 10th Workshop on Water Waves and Floating Bodies, Oxford, UK, pp 57–60

10. Contento G, Casole S (1995) On the generation and propagation of waves in 2D numerical wave tanks. In: Proceedings of the 5th International Offshore and Polar Engineering Conference, vol III, pp 10–18
11. Contento G, Codiglia R (2001) Non linear free surface induced pressure on a submerged horizontal circular cylinder at low Keulegan-Carpenters numbers. Appl Ocean Res 23:175–185
12. Dean WR (1948) On the reflection of surface waves by a submerged circular cylinder. Proc Camb Phil Soc 483–491
13. Dean RG, Dalrymple RN (1984) Water Wave Mechanics for Engineers and Scientists. World Scientific Advanced Series on Ocean Engineering, Prentice Hall Inc., Englewood Cliffs NJ
14. Grue J (1992) Nonlinear water waves at a submerged obstacle or bottom topography. J Fluid Mech 244:455–476
15. Grue J, Granlund K (1988) Impact of nonlinearity upon waves travelling over a submerged cylinder. In: Proceedings of the 3rd Workshop on Water Waves and Floating Bodies, Woods Hole, M.A. Dept. of Ocean Engineering, Mass. Inst of Technology, pp 57–60
16. Haller G (2005) An objective definition of a vortex. J Fluid Mech 525:1–26
17. Higuera P, Lara LJ, Losada IJ (2013) Realistic wave generation and active wave absorption for Navier-Stokes models application to OpenFOAM. Coast Eng 71:102–118
18. Hirt CW, Nichols BD (1981) Volume of fluid (VOF) method for the dynamics of free boundaries. J Comput Phys 39:201–225
19. Hunt J, Wray A, Moin P (1988) Eddies, strem, and convergent zones in turbulent flows. Center Turbulence Res Report CTR-S88
20. Jacobsen NG, Fuhrman DR, Fredsøe J (2012) A wave generation toolbox for the open-source CFD library: OpenFOAM. Int J Num Methods Fluids 70(9):1073–1088
21. Longuet-Higgins MS (1970) Steady currents induced by oscillations around islands. J Fluid Mech 42:701–720
22. Lupieri G, Contento G (2015) Numerical simulations of 2-D steady and unsteady breaking waves. Ocean Eng 106:298–316
23. Lupieri G, Contento G (2016) A numerical study on the viscous effects of waves travelling past a weakly submerged cylinder. To appear on Brodogradnja/Shipbuilding 67(4):61–79
24. Lupieri G, Puzzer T, Contento G (2014) Numerical study of the wave-wave interaction by viscous flow simulation with OpenFoam. The 21th Symposium Theory and Practice of Shipbuilding SORTA, Baška, Island of Krk, Croatia
25. Morison JR, O'Brien MP, Johnson JW, Schaaf SA (1950) The force exerted by surface waves on piles. Petrol Trans (Am Inst Min Eng) 189:149–154
26. Ogilvie TF (1963) First and second order forces on a cylinder submerged under a free surface. J Fluid Mech 16:451–472
27. Specialist Committee on CFD in Marine Hydrodynamics (2014) Proceedings—Volume II. 27th International Towing Tank Conference (ITTC), Copenhagen
28. OpenFOAM (2012) OpenFoam user guide. OpenCFD Ltd
29. Oshkai P, Rockwell D (1999) Free surface wave interaction with a horizontal cylinder. J Fluids Struct 13:935–954
30. Otsuka K, Ikeda Y (1996) Estimation of inertia forces on a horizontal circular cylinder in regular and irregular waves at low Keulegan-Carpenter numbers. Appl Ocean Res 18:145–156
31. Riley N (1971) Stirring of a viscous fluid. Z Angew Math Phys 22:645–653
32. Riley N (1978) Circular oscillations of a cylinder in a viscous fluid. Z Angew Math Phys 29:439–449
33. Riley N, Yan B (1996) Inviscid fluid flow around a submerged circular cylinder induced by free-surface travelling waves. J Eng Math 30:587–601
34. Rusche H (2002) Computational fluid dynamics of dispersed two—phase flows at high phase fractions. Imperial College of Science, Technology and Medicine, London
35. Schønberg T, Chaplin JR (2001) Computation of Non-Linear Wave Reflections and Transmissions from a Submerged Horizontal Cylinder. In: Proceedings of the Eleventh (2001) International Offshore and Polar Engineering Conference, vol III, pp 280–287
36. Stansby PK (1993) Forces on a circular cylinder in elliptical orbital flows at low Keulegan-Carpenter numbers. Appl Ocean Res 15:281–292
37. Stansby PK, Smith PA (1991) Viscous forces on a circular cylinder in orbital flow at low Keulegan-Carpenter numbers. J Fluid Mech 229:159–171
38. Swan C (2014) Group discussion on wave quality in wave basins and accurate models for the design wave kinematics. 27th International Towing Tank Conference (ITTC), Copenhagen
39. Tsai WT, Yue DKT (1996) Computation of non linear free-surface flows. Annu Rev Fluid Mech 28:249–278
40. Vada T (1987) A numerical solution of the second-order wave-diffraction problem for a submerged cylinder of arbitrary shape. J Fluid Mech 174:23–37
41. Wu GX, Eatock Taylor R (1990) The second order diffraction force on a horizontal cylinder in finite water depth. Appl Ocean Res 12:106–111
42. Yeung RW, Vaidhyanathan M (1992) Non-linear interaction of water waves with submerged obstacles. Int J Num Methods Fluids 14:1111–1130
43. Zhang C, Shen L, Yue DKP (1999) The mechanism of vortex connection at a free surface. J Fluid Mech 384:207–241